

# Streamline pathology foundation model by cross-magnification distillation

Ziyu Su<sup>a\*</sup>, Abdul Rehman Akbar<sup>a†</sup>, Usama Sajjad<sup>a†</sup>, Anil V. Parwani<sup>a</sup>, Muhammad Khalid Khan Niazi<sup>a</sup>

<sup>a</sup>Department of Pathology, College of Medicine, The Ohio State University Wexner Medical Center, Columbus, OH, USA

\*Correspondence: [ziyu.su@osumc.edu](mailto:ziyu.su@osumc.edu) (Z.S.)

†These authors contributed equally to this work.

## Abstract

Foundation models (FM) have transformed computational pathology but remain computationally prohibitive for clinical deployment due to their massive parameter counts and high-magnification processing requirements. Here, we introduce XMAG, a lightweight FM developed through cross-magnification distillation that transfers knowledge from state-of-the-art 20x magnification teacher to an efficient 5x magnification student architecture. XMAG employs a compact backbone and operates entirely at 5x, requiring 11.3 times fewer patches per whole slide image (WSI) compared to existing approaches. Our novel distillation framework incorporates dual-level knowledge transfer, aligning both global image representations and local spatial features across magnification levels through carefully designed projection heads and spatial token mapping. We trained XMAG on 3.49 million images curated from publicly available datasets and evaluated performance across six clinically relevant histopathology analysis tasks spanning multiple cancer types. XMAG achieved diagnostic accuracy within 1% of substantially larger foundation models while delivering 30-fold processing acceleration, reaching 8.8 WSIs per minute processing speed. Our cross-institutional validation confirmed robust generalization. Further, we developed an end-to-end training strategy to further boost our model's performance to approach the larger FMs' performance. These results establish cross-magnification distillation as a viable approach for deploying FM capabilities in resource-constrained clinical environments, potentially enabling real-time pathology AI integration.

**Keywords:** Computational Pathology, Foundation Model, Self-supervised Learning, Knowledge Distillation

## Introduction

Computational pathology (CPath) has emerged as a cornerstone of modern diagnostic medicine<sup>1,2</sup>, yet a fundamental challenge persists: achieving both high diagnostic accuracy and the rapid processing speeds required for clinical integration. Current CPath workflows<sup>3-7</sup> face a critical bottleneck where the time required for AI analysis often exceeds the pace of clinical decision-making, particularly in time-sensitive applications such as intraoperative consultations and high-throughput screening programs where pathologists require near real-time feedback<sup>8</sup>.

Foundation models (FMs) have revolutionized CPath by achieving unprecedented diagnostic accuracy across diverse histopathological tasks<sup>3-5</sup>. However, state-of-the-art models operate at high magnification (40-20x) with massive parameter counts—UNI2<sup>3</sup> (682M parameters), Virchow2<sup>9</sup> (632M parameters), and Gigapath<sup>5</sup> (1.1B parameters)—creating substantial computational demands that

effectively preclude clinical deployment. These computational requirements are particularly problematic for on-premises deployment in hospital environments, where data privacy regulations and institutional policies often mandate local processing of sensitive patient information on resource-constrained infrastructure.

The computational challenge is fundamentally rooted in a magnification-efficiency trade-off. Higher magnification imaging captures more detailed morphological features but requires exponentially more patches for analysis—20x magnification necessitates processing 16-fold more patches than 5x magnification for the same tissue area (see Figure 1a). Current approaches assume that high magnification is essential for competitive diagnostic performance, raising a critical question: can comparable accuracy be achieved at lower magnification using more efficient architectures?<sup>10,11</sup>

Knowledge distillation presents a promising avenue for addressing these challenges by enabling compact models to learn from larger, more capable teachers<sup>12,13</sup>. However, no framework currently exists for cross-magnification knowledge transfer in CPath—an approach that could potentially combine the detailed feature representations learned at high magnification with the computational efficiency of low-magnification analysis. Such a framework could not only improve processing efficiency but also overcome data limitations by transferring learned representations from models trained on larger datasets.

Here, we introduce XMAG (Cross-Magnification Distillation), a novel framework that transfers knowledge from a 20x magnification teacher model to a compact 5x magnification student model with only 86M parameters. XMAG operates entirely at 5x magnification during deployment, compressing each WSI into about 12 times fewer patches than under 20x, while maintaining >99% of 20x FMs' diagnostic accuracy. The compact architecture and reduced patch requirements enable end-to-end training for WSI-level classification<sup>14</sup>, allowing task-specific adaptation that is previously challenging with larger models due to memory constraints.

Remarkably, we systematically assembled and curated a training dataset of 3.49 million patches span across sixteen different cancer types from publicly available sources. XMAG achieves performance comparable to state-of-the-art FMs trained on larger private datasets<sup>3</sup>, demonstrating that cross-magnification distillation enables efficient knowledge transfer that compensates for dataset scale differences. This combination of our curated public dataset and distillation framework democratizes access to high-performance pathology AI.

We demonstrate XMAG's capabilities across six clinically relevant tasks, four in WSI-level and two in local patch-level, spanning multiple cancer types, with cross-institutional validation confirming robust generalization. XMAG achieves processing speeds of 8.8 WSIs per minute representing an 8-30 fold improvement over existing foundation models, while maintaining diagnostic accuracy of about 99% of substantially larger models. These results represent a paradigm shift from research-grade tools toward clinically deployable AI systems, potentially enabling the first practical integration of foundation model capabilities into routine pathological practice.

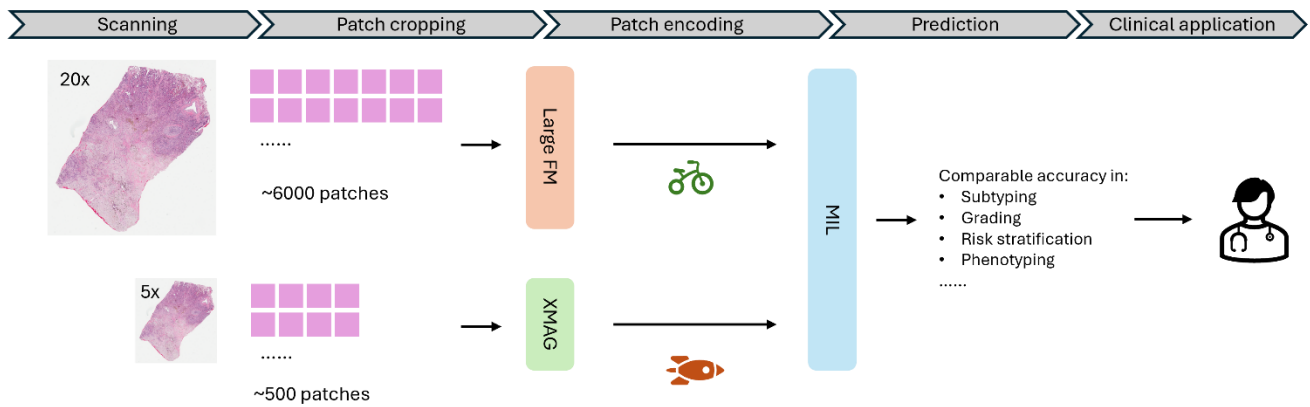
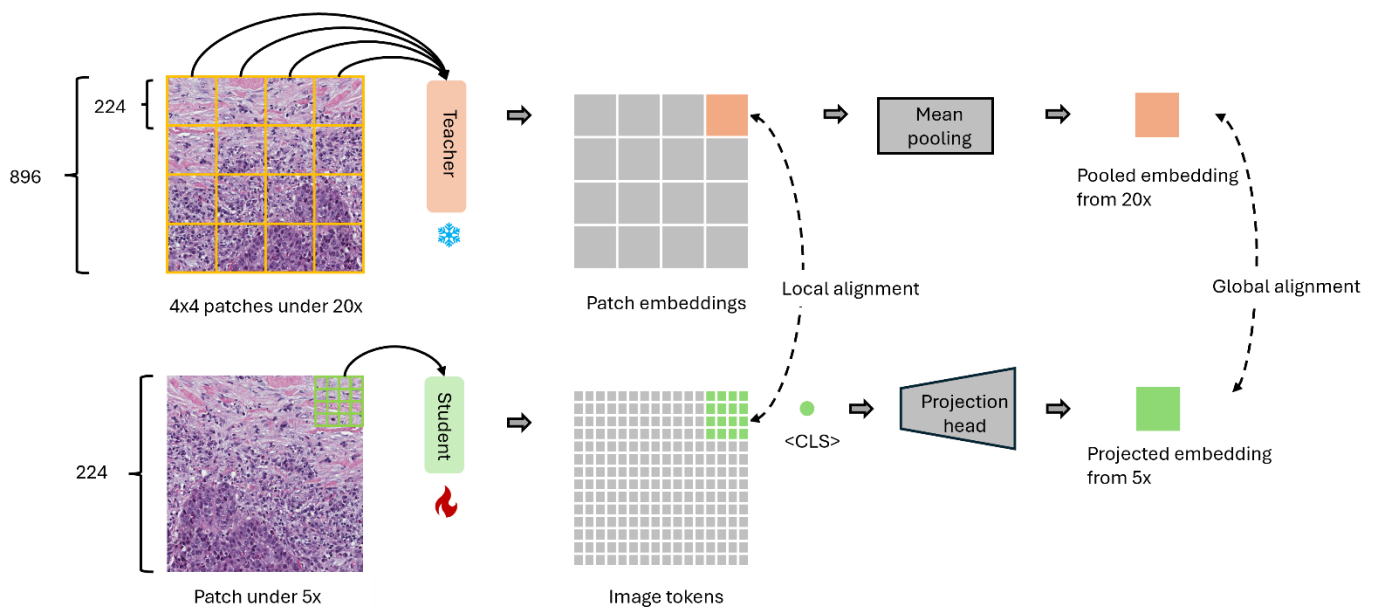
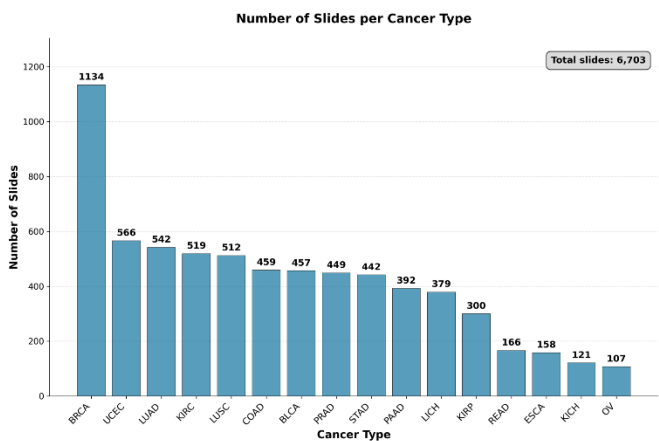
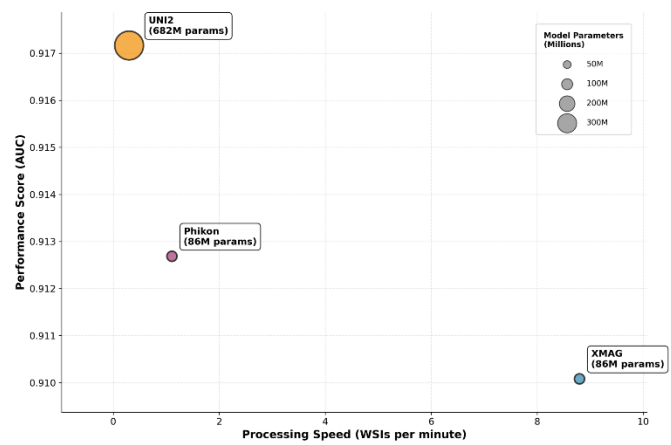
**a****b****c****d**

Figure 1. Overview of the XMAG. XMAG transfers knowledge from high-magnification foundation models to compact low-magnification architectures, achieving comparable diagnostic performance with dramatically improved processing efficiency across multiple clinical tasks. **a.** Traditional 20× approaches process ~6,000 patches per WSI through large foundation models, while XMAG operates at 5× magnification with ~500 patches, maintaining diagnostic accuracy with improved efficiency on various tasks. **b.** Cross-magnification distillation architecture. Teacher model (UNI2) processes 4×4 grids of sub-patches, generating embeddings for global and local alignment.

Student model (DINOv2-ViT-B) processes 224×224 patches with spatial token mapping and projection heads for dual-level knowledge transfer. **c.** Our pretraining dataset comprises 6,703 WSIs across 15 cancer types from public sources, totaling 3.49 million patches for distillation training. **d.** XMAG achieves optimal balance between diagnostic performance (average AUC) and processing speed (8.8 WSIs/minute) compared to existing foundation models. Bubble size indicates parameter count.

## Results

### WSI-level classification

WSI classification represents the pinnacle of computational pathology applications, directly mirroring the diagnostic decision-making process that pathologists perform in clinical practice<sup>15</sup>. The ultra-high resolution of WSIs (typically exceeding 100,000 × 100,000 pixels) necessitates multiple instance learning (MIL) approaches, where WSIs are tessellated into manageable patches, encoded by FMs, and subsequently aggregated through MIL classifiers for slide-level predictions<sup>6</sup>. Due to GPU memory constraints, patch encoding and MIL classification operate as decoupled processes during training—FMs run in inference mode while only MIL aggregation layers undergo task-specific optimization. This architectural constraint places paramount importance on the representational quality of pretrained FMs, as their frozen feature extraction capabilities directly determine downstream classification performance without the ability to adapt to specific diagnostic tasks.

We benchmarked XMAG against two established pathology FMs using attention-based MIL (ABMIL)<sup>16</sup>: UNI2<sup>3</sup>, a state-of-the-art 682M parameter model, and Phikon<sup>17</sup>, a more lightweight 86M parameter architecture. Both comparison models were developed to be operated at 20x magnification, while XMAG processes 5x magnification patches.

We selected the following tasks as our WSI-level benchmarks: non-small cell lung cancer (NSCLC) subtyping, renal cell carcinoma (RCC) subtyping, prostate cancer ISUP grading, and breast cancer Oncotype-DX (BRCA-ODX) stratification. For all experiments, XMAG used 224×224 patch size under 5x, and the other two models use 256×256 patch size under 20x following their original implementations.

For NSCLC subtyping, we classified WSIs into lung adenocarcinoma (LUAD) and lung squamous cell carcinoma (LUSC) using the Clinical Proteomic Tumor Analysis Consortium (CPTAC) dataset. Under five-fold cross-validation, XMAG achieved an average area under the receiver operating characteristics curve (AUC) of  $0.941 \pm 0.015$  (95% CI 0.922-0.942). For RCC subtyping, we performed three-way classification distinguishing papillary renal cell carcinoma (PRCC), chromophobe renal cell carcinoma (ChRCC), and clear cell renal cell carcinoma (ccRCC). We trained the MIL models using five-fold cross-validation on the TCGA RCC dataset and evaluated all models on an external testing cohort from Dartmouth-Hitchcock Medical Center (DHMC)<sup>18</sup>. XMAG achieved an average AUC of  $0.986 \pm 0.009$  (95% CI 0.977-0.993) on the external test set, demonstrating robust generalization across institutions. For prostate cancer ISUP grading, we classified prostate biopsies into ISUP grades 0-5 using the PANDA challenge dataset<sup>19</sup>. Under five-fold cross-validation, XMAG achieved an average AUC of  $0.910 \pm 0.003$  (95% CI 0.907-0.914). For BRCA-ODX stratification, we classified breast cancer cases into high or low recurrence risk based on Oncotype DX genetic test score thresholds (>25). We trained MIL models using five-fold cross-validation on the TCGA breast cancer dataset and tested performance on an

independent cohort from The Ohio State University Wexner Medical Center (OSUWMC)<sup>20,21</sup>. XMAG achieved an average AUC of  $0.776 \pm 0.006$  (95% CI 0.758-0.795) on the testing set.

Remarkably, across most of the benchmark tasks, XMAG's performance was statistically indistinguishable ( $p>0.05$ ) from the inefficient 20x FM (Figure 2). Only on the ISUP grading task did comparison models achieve significantly superior performance, with Phikon reaching an AUC of 0.926 (+0.009 over XMAG,  $p<0.01$ ) and UNI2 achieving 0.936 (+0.019 over XMAG,  $p<0.001$ ). Conversely, in RCC subtyping and BRCA-ODX stratification, XMAG exceeded comparison models in F1-score metrics. For RCC subtyping, XMAG achieved an F1-score of 0.916, outperforming Phikon by +0.104 ( $p<0.01$ ) while showing comparable performance to UNI2 (+0.003,  $p>0.05$ ). In BRCA-ODX stratification, XMAG demonstrated F1-scores of 0.844, with non-significant improvements over both Phikon (+0.039,  $p>0.05$ ) and UNI2 (+0.009,  $p>0.05$ ). These results suggest that the cross-magnification distillation framework not only preserves diagnostic accuracy but may enhance certain aspects of feature representation through multi-scale integration. These results demonstrate that our 5x FM achieves clinical-grade performance while operating with significantly reduced computational overhead—a critical advancement for real-world pathology workflow integration. More detailed comparison results can be found in Supplementary Table S1-4.

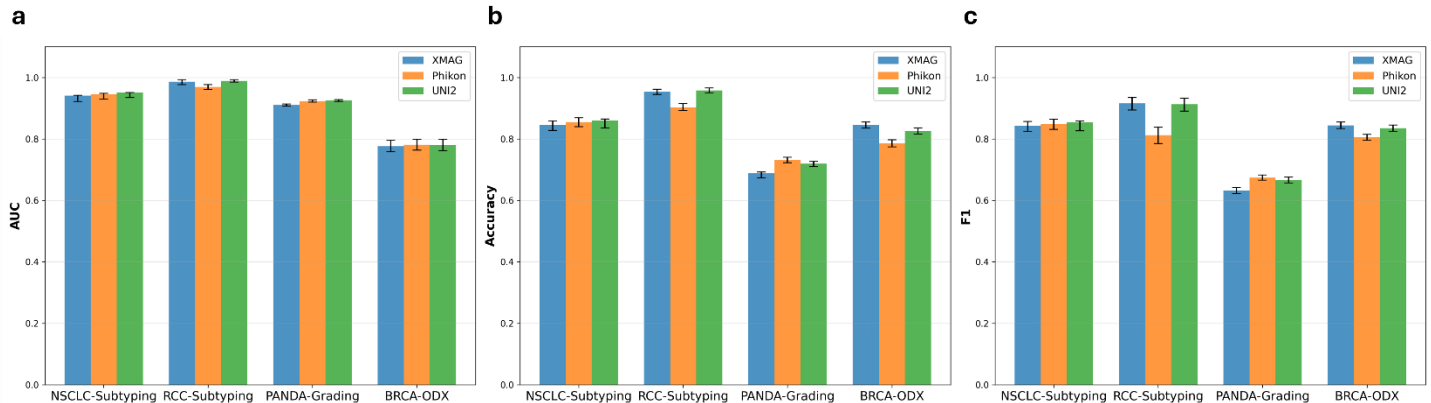


Figure 2. Performance on WSI-level classification tasks. **a-c.** AUC, accuracy, and F1-score comparisons between XMAG, Phikon, and UNI2 across four WSI classification benchmarks. Error bars represent 95% confidence intervals.

### Speed and scale comparison

The practical deployment of FMs in clinical pathology workflows demands not only high diagnostic accuracy but also computational efficiency compatible with real-time clinical decision-making. We systematically evaluated the computational performance of XMAG against established pathology FMs to assess clinical deployment feasibility.

In Figure 3a presents the average number of patches per WSI across our benchmark datasets (CPTAC-NSCLC, DHMC-RCC, PANDA, and OSUWMC-BRCA), demonstrating that 5x magnification requires substantially fewer patches than 20x magnification to represent entire WSIs—an average reduction of 11.3-fold across datasets. To quantify processing efficiency under realistic conditions, we simulated WSI analysis using representative patch counts derived from our benchmarking datasets: 554 patches of 224×224 pixels for 5× magnification (XMAG) and 6,260 patches for 20× magnification (comparison models). These values represent the averaged patch requirements across the four benchmark datasets at their respective magnifications, reflecting typical coverage differences in our experimental setting.

Under identical hardware conditions, XMAG demonstrated remarkable computational efficiency, requiring only 6.82 seconds for patch processing compared to 54.21 seconds for Phikon and 201.25 seconds for UNI2 (Figure 3b). This represents a 7.95-fold speedup over Phikon and a 29.51-fold acceleration compared to UNI2. Translating these processing times to clinical throughput metrics reveals the practical significance of these efficiency gains. XMAG achieves a processing rate of 8.80 WSIs per minute, substantially exceeding both Phikon (1.11 WSIs/minute) and UNI2 (0.30 WSIs/minute).

To contextualize these efficiency gains within the performance-accuracy landscape, we constructed a comprehensive comparison incorporating model parameters, processing speed, and average diagnostic performance across all four WSI-level classification tasks (Figure 1d). This analysis reveals XMAG's unique position in the efficiency-accuracy trade-off space: while maintaining 86M parameters—identical to Phikon—XMAG achieves nearly equivalent diagnostic performance (average AUC across NSCLC, RCC, ISUP, and BRCA-ODX tasks: 0.910 vs 0.913) with dramatically superior throughput. Compared to the larger UNI2 model (682M parameters, average AUC: 0.917), XMAG retains comparable accuracy while delivering 49-fold faster processing.

These results demonstrate that cross-magnification distillation enables a fundamental breakthrough in the clinical deployment paradigm for pathology FMs. By achieving clinically competitive diagnostic accuracy at processing speeds compatible with real-world pathology workflows, XMAG bridges the critical gap between research-grade model performance and clinical deployment requirements, potentially enabling the first practical integration of FM capabilities into routine pathological practice.

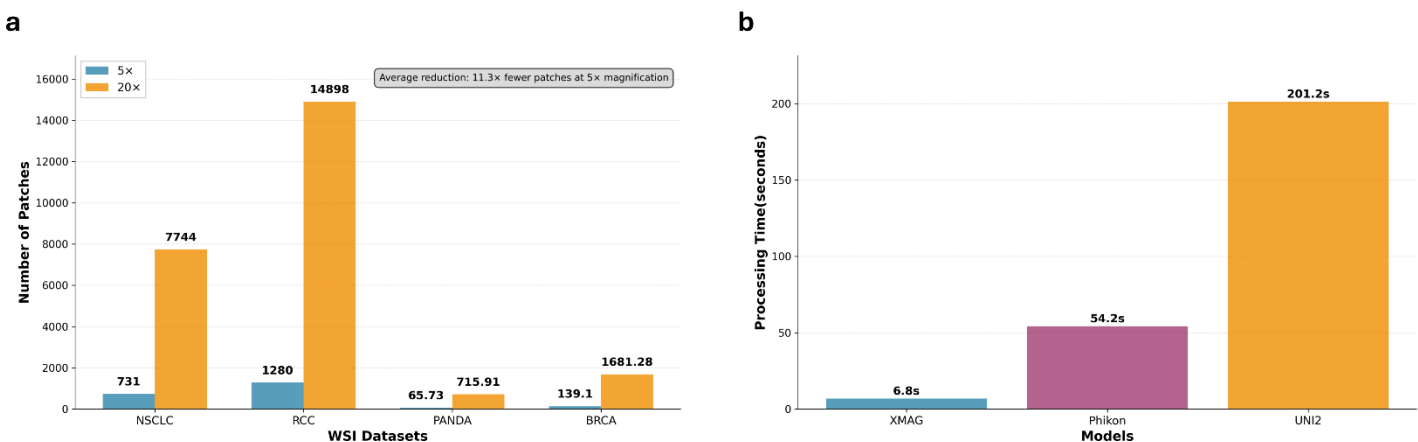


Figure 3. Computational efficiency of 5x and 20x models. **a.** Patch count comparison across WSI datasets showing 11.3-fold average reduction in patches required for 5x versus 20x magnification analysis. **b.** Processing time comparison demonstrating XMAG's superior efficiency with 29.5-fold and 6.8-fold speedups over UNI2 and Phikon, respectively.

### End-to-end integration enables task-specific adaptation

To evaluate whether joint optimization of FM and MIL components could enhance diagnostic performance, we implemented an end-to-end training framework that integrates XMAG with ABMIL (e2e-XMAG). This approach enables gradient flow from the MIL objective back through the FM<sup>14</sup>, allowing task-specific feature adaptation—a capability precluded by conventional frozen encoder pipelines due to memory constraints.

We benchmarked e2e-XMAG on prostate cancer ISUP grading, the most challenging task in our evaluation suite where XMAG exhibited the largest performance gap relative to 20x FMs. The end-to-end framework incorporates gradient checkpointing and selective layer unfreezing to manage memory requirements while enabling targeted adaptation of high-level feature representations.

e2e-XMAG demonstrated substantial performance improvements over the conventional frozen encoder approach (Table 1). Specifically, end-to-end training achieved increased AUC of 0.924 (+0.007,  $p<0.01$ ), accuracy of 0.713 (+0.025,  $p<0.01$ ), and F1-score of 0.654 (+0.027,  $p<0.05$ ). These gains represent statistically significant improvements across all metrics, indicating that task-specific adaptation effectively compensates for the reduced model capacity relative to larger FMs.

Remarkably, e2e-XMAG performance approaches that of substantially larger models while maintaining computational efficiency advantages (Table 1). These results demonstrate that cross-magnification distillation combined with end-to-end optimization provides a viable path toward deploying FM capabilities in resource-constrained clinical environments without substantial diagnostic performance penalties.

Table 1. Performance comparison on prostate cancer ISUP grading (PANDA dataset) between end-to-end XMAG and conventional MIL pipelines with frozen foundation models. Values represent mean  $\pm$  standard deviation across five-fold cross-validation.

	AUC	Accuracy	F1-score
e2e-XMAG	0.924 $\pm$ 0.002	0.713 $\pm$ 0.005	0.654 $\pm$ 0.006
XMAG-ABMIL	0.910 $\pm$ 0.003	0.688 $\pm$ 0.010	0.632 $\pm$ 0.012
Phikon-ABMIL	0.923 $\pm$ 0.002	0.731 $\pm$ 0.009	0.674 $\pm$ 0.017
UNI2-ABMIL	0.925 $\pm$ 0.004	0.719 $\pm$ 0.010	0.666 $\pm$ 0.010

## Patch-level classification

Histopathological phenotyping—the identification and classification of distinct tissue morphologies—is fundamental to pathological diagnosis, with pathologists routinely examining tissue architecture across multiple magnifications to characterize cellular and structural phenotypes. In CPath, this critical diagnostic process is typically implemented through patch-level classification, where image patches extracted from WSIs are systematically categorized into distinct phenotypic classes. This task serves as a critical benchmark for evaluating whether FMs can extract semantically meaningful features with genuine histological relevance.

We assessed the tissue phenotyping performance of XMAG using two established patch-level classification datasets: SPIDER-Breast, SPIDER-CRC<sup>22</sup>. These datasets provide comprehensively annotated patches extracted from breast and colorectal cancer WSIs, respectively. Each patch is labeled at 224 $\times$ 224 pixels under 20x magnification, with the surrounding 1120 $\times$ 1120 pixel region available. To simulate 5x magnification patches for XMAG evaluation, we extracted 896 $\times$ 896 pixel regions centered on each patch and downsampled them to 224 $\times$ 224 pixels. SPIDER-Breast contains eighteen distinct tissue categories, while SPIDER-CRC encompasses thirteen categories.

We conducted linear probing experiments to benchmark XMAG against two state-of-the-art 20x FMs: UNI2 and Phikon. For each model, we appended a trainable linear classifier while keeping the FM weights frozen during training, ensuring fair comparison of learned representations.

On the official testing set, XMAG achieved AUC value of 0.988 (95% CI 0.988-0.989) for SPIDER-Breast. In comparison, Phikon achieved an AUC of 0.992 (+0.004,  $p>0.1$ ) and UNI2 achieved an AUC of 0.994 (+0.006,  $p=0.05$ ). On the SPIDER-CRC, XMAG achieved AUC value of 0.990 (95% CI 0.990-0.991). In comparison, Phikon achieved an AUC of 0.994 (+0.004,  $p=0.011$ ) and UNI2 achieved an AUC of 0.994 (+0.004,  $p=0.039$ ). While these results represent a modest decrease compared to the 20x FMs. This modest performance reduction likely stems from label-irrelevant phenotypic information in the peripheral regions of 5x patches. SPIDER dataset annotations are based on the central 224×224 region of each patch, while the surrounding tissue areas incorporated when downscaling from 20x to 5x magnification may contain phenotypes unrelated to the assigned label. More detailed results can be found in Figure 4 and Supplementary Table S5 and Table S6.

To visualize the learned feature representations, we applied t-SNE (t-distributed stochastic neighbor embedding)<sup>23</sup> dimensionality reduction to XMAG and UNI2's patch embeddings (Figure 5). The resulting two-dimensional embedding space revealed distinct clustering of patches according to their phenotypic categories, indicating that XMAG successfully captures histologically relevant features despite operating at reduced magnification. The clear separation between tissue types demonstrates that the cross-magnification distillation framework preserves critical discriminative information necessary for accurate phenotypic classification.

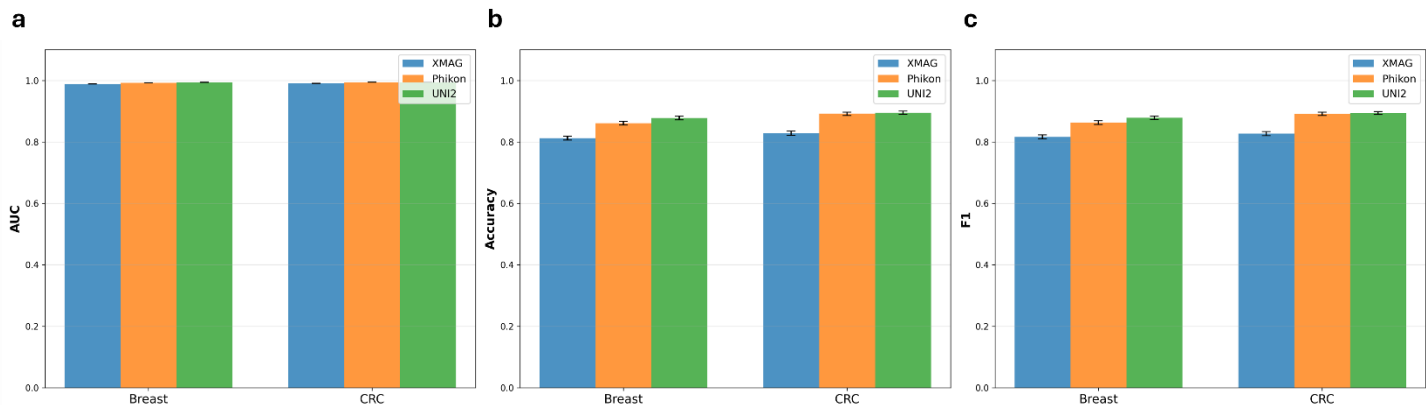


Figure 4. Performance on patch-level classification tasks. **a-c.** AUC, accuracy, and F1-score comparisons between XMAG, Phikon, and UNI2 across two patch-level classification benchmarks. Error bars represent 95% confidence intervals.

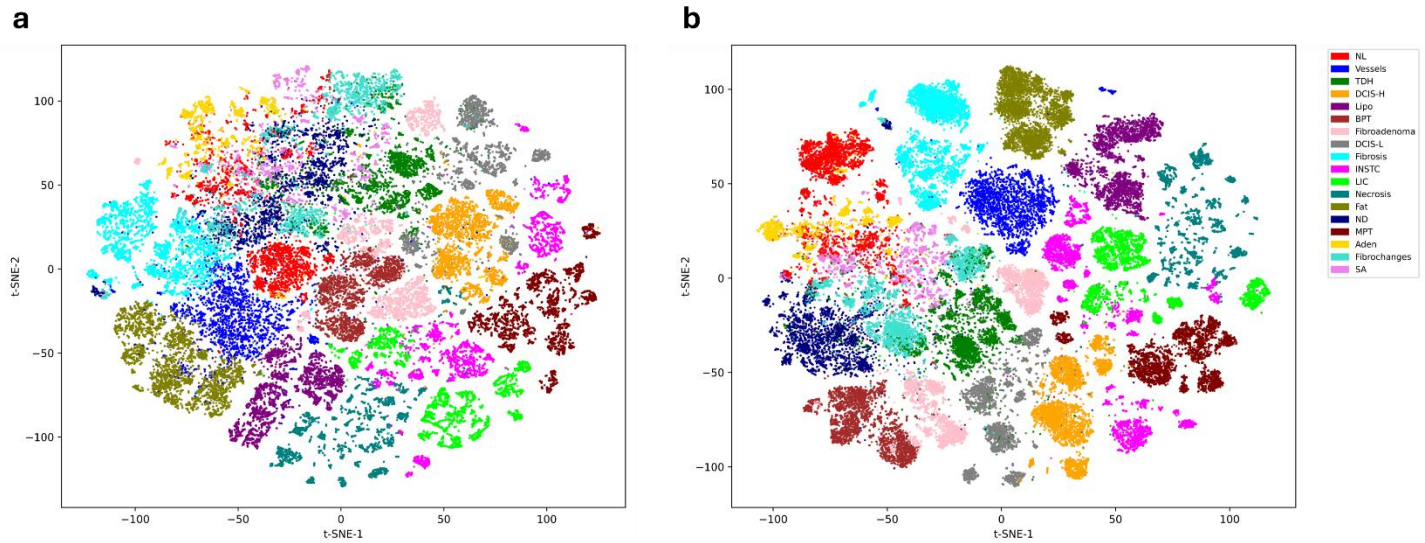


Figure 5. Two-dimensional feature space visualization of XMAG and UNI2 using t-SNE. Patches from the SPIDER dataset are embedded using the XMAG and UNI2 under the inference mode separately, and then mapped to two-dimensional space using the t-SNE technique. **a-b.** Visualization of patch features from SPIDER-Breast dataset encoded by XMAG and UNI2, respectively. **c-d.** Visualization of patch features from SPIDER-CRC dataset encoded by XMAG and UNI2, respectively.

## Discussion

The persistent gap between CPath research achievements and clinical deployment represents one of the most significant barriers to realizing the transformative potential of AI in diagnostic medicine<sup>24</sup>. While FMs have demonstrated unprecedented accuracy across diverse histopathological tasks, their substantial computational requirements create processing bottlenecks that fundamentally limit clinical integration. These computational demands are particularly problematic for on-premises deployment, which is often required in healthcare settings due to data privacy regulations and institutional policies that restrict cloud-based processing of sensitive patient information<sup>25</sup>. Our results demonstrate that cross-magnification distillation provides a viable pathway to bridge this deployment gap, enabling XMAG to achieve 7-30 folds faster WSI processing speed while maintaining diagnostic performance within 1% of substantially larger models. This represents a paradigm shift from research-grade tools toward clinically viable AI systems, potentially enabling real-time pathology applications in resource-constrained environments where local deployment and rapid diagnostic turnaround is essential.

The technical innovation of cross-magnification distillation addresses a counterintuitive challenge in computational pathology: that detailed morphological information captured at high magnification can be effectively transferred to models operating at substantially lower resolution. This finding challenges the prevailing assumption that competitive diagnostic performance necessitates high-magnification analysis with its associated computational overhead. Our dual-level alignment approach—combining global feature matching with local spatial correspondence—enables the transfer of fine-grained morphological knowledge while operating with 16-fold fewer patches per WSI. This approach builds upon the broader knowledge distillation<sup>13</sup> and ViT<sup>26</sup> design literature but introduces novel spatial alignment mechanisms specifically designed for the multi-scale nature of histopathological analysis. The success of this cross-resolution knowledge transfer suggests that much of the diagnostic information captured by high-magnification models can be preserved through appropriately designed distillation frameworks.

A critical advantage of our approach lies in its data efficiency and accessibility. XMAG achieves competitive performance using a training dataset of 3.49 million patches curated entirely from publicly available sources, that is substantially smaller than the proprietary datasets typically required for state-of-the-art models<sup>3</sup>. This data efficiency stems from the knowledge distillation framework, which leverages representations learned by teacher models trained on larger datasets, effectively democratizing access to high-performance pathology AI. This contrasts sharply with the current trend toward increasingly large, private datasets that create barriers to entry for academic institutions and smaller research groups. Our publicly curated dataset and distillation methodology provide a foundation for broader community engagement in CPath research.

The computational efficiency of XMAG enables enhanced training flexibility for downstream applications. While full end-to-end optimization of FM with MIL remains challenging due to memory constraints, XMAG's reduced computational footprint allows for selective fine-tuning approaches using gradient checkpointing techniques. Our experiments on prostate cancer ISUP grading demonstrate that partial end-to-end optimization can yield meaningful performance improvements. This suggests potential for more sophisticated training strategies that could further improve task-specific performance as memory-efficient training techniques continue to advance.

Several limitations warrant consideration in interpreting these results. First, our evaluation reveals that certain diagnostic tasks may inherently require high-magnification analysis, as evidenced by the performance gap in prostate cancer grading where cellular-level morphological details are critical for accurate ISUP scoring. This suggests that future approaches may need to incorporate multi-resolution strategies that dynamically select appropriate magnification levels based on diagnostic requirements<sup>27</sup>. Second, the distillation framework creates a performance ceiling effect, where student model capabilities are fundamentally limited by teacher model performance. Integration of additional self-supervised objectives such as masked image modeling or contrastive learning could potentially overcome this limitation. Third, current memory-efficient training techniques still require trade-offs between computational efficiency and full end-to-end optimization, indicating that further advances in training methodologies will be needed to fully realize the potential of joint foundation model-MIL optimization. Finally, our evaluation focuses on diagnostic accuracy metrics, but clinical deployment requires validation of robustness across diverse imaging conditions, scanner variations, and patient populations that may not be fully captured in curated research datasets<sup>28</sup>.

In summary, XMAG addresses critical barriers to clinical deployment of computational pathology by delivering foundation model performance with dramatically improved efficiency and practical deployability. The substantial processing acceleration enables real-time diagnostic workflows, while the compact architecture facilitates on-premises deployment in hospital environments with data privacy constraints and limited computational resources. By maintaining diagnostic accuracy comparable to state-of-the-art models while operating at clinically viable speeds, XMAG represents a practical step toward integrating AI-powered pathology analysis into routine clinical practice, potentially accelerating diagnostic turnaround times and improving patient care delivery.

## Methods

### Pretraining dataset

We established a cross-magnification pretraining dataset with about 3.49 million patches under 5x magnification from hematoxylin and eosin (H&E) WSIs. The dataset is a multi-cancer dataset created from the publicly available WSIs from TCGA (see Figure 1c). It incorporates sixteen different cancer types and 6703 WSIs. Based on our distillation approach, we require each 5x patch has its equivalent 20x region available. Thus, when creating the dataset, we cropped patches in 896×896 pixel size under 20x magnification and then downscale them into 224×224 to create the 5x patches. Before resizing, we divide the 896×896 patch into 4 by 4 grids to generate sixteen 224×224 patches under 20x. In summary, each 5x patch corresponds to sixteen 20x patches during the cross-magnification distillation.

### Self-supervised training using cross-magnification distillation

Knowledge distillation is a technique where a lightweight student model align its extracted feature to a powerful teacher model, so that the student can achieve similar performance as the teacher model does with fewer parameter. To enable knowledge transfer from high-magnification foundation models to computationally efficient low-magnification architectures, we developed a novel cross-magnification distillation framework that addresses the fundamental challenge of aligning features across different spatial resolutions and magnification levels. Specifically, our method establishes correspondence between 16 non-overlapping 20x patches and a single spatially-equivalent 5x patch, enabling the distillation of fine-grained morphological knowledge into a more efficient representation. Our model architecture is outline in Figure 1b.

#### Teacher-Student Architecture

Let  $X^{20\times} \in \mathbb{R}^{896 \times 896 \times 3}$  denote a high-magnification patch at 20x and  $X^{5\times} \in \mathbb{R}^{224 \times 224 \times 3}$  represent the corresponding low-magnification patch at 5x, where both patches capture the same tissue region. Our teacher network is UNI2, a state-of-the-art FM pretrained with 100 million patches of 256×256 under 20x. It applies a ViT-h backbone with 682 million parameters. The teacher network  $f_T$  processes  $X^{20\times}$  by first decomposing it into 16 non-overlapping sub-patches:

$$X^{20\times} = \{x_i^{20\times}\}_{i=1}^{16}, \quad x_i^{20\times} \in \mathbb{R}^{224 \times 224 \times 3}$$

Each sub-patch is independently encoded to produce high-dimensional patch features:

$$h_i^T = f_T(x_i^{20\times}) \in \mathbb{R}^{d_T}, \quad i = 1, \dots, 16$$

where  $d_T = 1536$  is the teacher embedding dimension.

Our student network is a DINOV2-ViT-B<sup>29</sup> has 86 million parameters. The student network  $f_S$  processes the corresponding 5x patch through a single forward pass, yielding a class token and spatial patch tokens:

$$c^S, \{t_j^S\}_{j=1}^{256} = f_S(X^{5\times})$$

where  $c^S \in \mathbb{R}^{d_S}$  is the global class token and  $t_j^S \in \mathbb{R}^{d_S}$  are patch tokens with  $d_S = 768$ .

#### Spatial Resolution Alignment

To establish spatial correspondence between teacher and student representations, we perform spatial pooling on the student's 256 patch tokens, which are arranged in a 16×16 spatial grid. We reshape and aggregate these tokens into 16 spatially-aligned features through 4×4 average pooling:

$$T^S = \text{reshape} \left( \{t_j^S\}_{j=1}^{256}, 16 \times 16 \right) \in \mathbb{R}^{16 \times 16 \times d_S}$$

$$h_i^S = \frac{1}{16} \sum_{p=1}^4 \sum_{q=1}^4 T_{4i_r+p, 4i_c+q}^S, \quad i = 1, \dots, 16$$

where  $i_r$  and  $i_c$  denote the row and column indices corresponding to the  $i$ -th spatial region (see Figure 1b).

### Dimension Matching through Projection Heads

To align the dimensional disparity between teacher ( $d_T = 1536$ ) and student ( $d_S = 768$ ) representations, we employ learnable projection heads. For global features, a two-layer MLP  $g_{global}$  projects the student class token to  $....$  dimensional space:

$$z_{global}^S = g_{global}(c^S) = W_2 \cdot \text{GELU}(BN(W_1 c^S + b_1)) + b_2$$

where  $W_1 \in \mathbb{R}^{d_T \times d_S}$ ,  $W_2 \in \mathbb{R}^{d_T \times d_T}$ , and  $BN$  denotes batch normalization.

Similarly, for local features, each spatially-aligned student feature is projected to  $...$  dimensional space:

$$z_i^S = g_{local}(h_i^S), \quad i = 1, \dots, 16$$

### Knowledge Distillation

Our distillation objective combines global and local alignment losses. The global teacher representation is obtained from by averaging spatial features:

$$h_{global}^T = \frac{1}{16} \sum_{i=1}^{16} h_i^T$$

The global distillation loss employs negative cosine similarity:

$$L_{global} = -\frac{h_{global}^T \cdot z_{global}^S}{\|h_{global}^T\|_2 \|z_{global}^S\|_2}$$

The local distillation loss aligns spatially-corresponding features:

$$L_{local} = -\frac{1}{16} \sum_{i=1}^{16} \frac{h_i^T \cdot z_i^S}{\|h_i^T\|_2 \|z_i^S\|_2}$$

The total distillation loss is:

$$L = \lambda_{global} L_{global} + \lambda_{local} L_{local}$$

where  $\lambda_{global} = 1$  and  $\lambda_{local} = 0.5$  are weighting coefficients.

### Training details

We employ data augmentation ensuring identical transformations are applied to both teacher and student inputs to maintain spatial correspondence. The student parameters are optimized using AdamW with learning rate  $5 \times 10^{-4}$  and cosine annealing schedule. An exponential moving average

(EMA) of student parameters is maintained to stabilize the training. After training, the EMA student network is saved as our finalized XMAG model. Finally, our model was trained for 30260 iterations using 24 NVIDIA A100-40GB GPUs.

## WSI-level classification

### *Multiple Instance Learning*

For all WSI-level classification tasks, we employ MIL as the underlying framework. Each WSI is first tessellated into non-overlapping patches of  $224 \times 224$  pixels at 5x magnification. We then utilize XMAG in inference mode to encode all patches from each WSI into patch-level embeddings:

$$h_i = f_{XMAG}(x_i^{5 \times}), \quad i = 1, 2, \dots, M$$

where  $f_{XMAG}(\cdot)$  denotes the XMAG,  $h_i \in \mathbb{R}^{768}$  represents the patch embedding derived from XMAG's class token,  $x_i$  is the  $i$ -th patch, and  $N$  indicates the total number of patches extracted from a WSI.

The resulting patch embeddings  $\{h_i\}_{i=1}^M$  are then aggregated into WSI-level predictions using ABMIL<sup>16</sup>, which learns to weight patch contributions based on their relevance to the classification task. During training, XMAG parameters remain frozen while only the ABMIL aggregation network is optimized for each downstream task.

### *End-to-end training of MIL with XMAG*

Conventional MIL pipelines decouple FM inference from downstream task training due to GPU memory constraints. This separation limits the model's ability to learn task-specific features, as patch encodings are computed in a separate preprocessing step without gradient flow from the MIL objective. This architectural limitation prevents FMs from adapting their representations to specific downstream tasks during MIL training.

GPU memory consumption in end-to-end MIL training stems from two primary factors: (1) the large number of patches extracted from WSIs at high magnification, and (2) the substantial memory footprint of large FMs storing intermediate activations during backpropagation. XMAG presents a unique opportunity to address both limitations simultaneously. Operating at 5x magnification, XMAG naturally requires fewer patches compared to 20x models, reducing the spatial complexity of MIL training. Additionally, XMAG's DINOv2-ViT-B backbone (86M parameters) is substantially more compact than state-of-the-art pathology foundation models, resulting in significantly reduced memory requirements for intermediate activations.

Building on these advantages, we developed end-to-end XMAG (e2e-XMAG) that integrates XMAG with ABMIL in a unified training framework. To further optimize GPU memory usage, we employ gradient checkpointing to trade computation for memory by discarding intermediate activations during forward passes and recomputing them as needed during backpropagation.

Our implementation incorporates selective layer fine-tuning based on empirical ablation studies. We freeze the first ten Vision Transformer blocks of XMAG while allowing the final transformer block to adapt during MIL training. This selective unfreezing strategy, determined through systematic ablation experiments, provides an optimal balance between task-specific adaptation and computational efficiency. The frozen early layers maintain the robust low-level feature representations learned during

cross-magnification distillation, while the trainable final layer enables task-specific feature refinement guided by the MIL objective.

The complete e2e-XMAG pipeline processes WSI patches through the partially-frozen XMAG encoder with gradient checkpointing, projects the resulting embeddings to the appropriate dimensionality for MIL aggregation, and jointly optimizes both the unfrozen XMAG parameters and ABMIL weights using the downstream classification loss. This end-to-end optimization enables the model to learn representations specifically tailored to each diagnostic task while maintaining the computational efficiency benefits of the cross-magnification distillation framework.

## Statistical Methods

Statistical significance of performance comparisons between methods was assessed using appropriate tests for each metric. For AUC comparisons, we employed DeLong's test to account for correlated ROC curves from the same test set. Accuracy differences were evaluated using McNemar's test for paired binary outcomes. F1-score comparisons were conducted using bootstrap hypothesis testing with 1,000 bootstrap samples. Confidence intervals (95% CI) for all metrics were calculated using bootstrap resampling with 1,000 iterations.

## Datasets Used in the Study

We evaluated XMAG across multiple publicly available and internal datasets spanning lung, renal, breast, colon, and prostate cancers.

- **TCGA-NSCLC:** The TCGA-NSCLC dataset is used for training NSCLC subtyping model. It contains 958 diagnostic whole-slide images (WSIs), including 492 lung adenocarcinoma (LUAD) slides and 466 lung squamous cell carcinoma (LUSC) slides. The dataset is available through the National Cancer Institute's Genomic Data Commons (GDC) portal (<https://portal.gdc.cancer.gov>).
- **CPTAC-NSCLC:** The CPTAC-NSCLC dataset is used for testing the NSCLC subtyping model. It provides matched proteogenomic and histopathology data, accessible via the GDC portal. After excluding normal cases, the dataset includes 668 LUAD slides and 306 LUSC slides. Data are publicly available via the GDC portal (<https://portal.gdc.cancer.gov>).
- **TCGA-RCC:** The TCGA-RCC dataset is used for training the RCC subtyping model. We employed the TCGA Kidney collections (*KICH*, *KIRC*, and *KIRP*), comprising 903 diagnostic WSIs from renal cell carcinoma patients. It includes 118 ChRCC slides, 288 PRCC slides, and 497 CCRCC slides. Data are publicly available via the GDC portal (<https://portal.gdc.cancer.gov>).
- **DHMC-RCC:** The DHMC-RCC dataset is used for testing the RCC subtyping model. We employed the published dataset from *Dartmouth-Hitchcock Medical Center* (DHMC) consisting of 563 WSIs from RCC patients. It includes This dataset was held out for testing only, and is available at <https://bmirds.github.io/KidneyCancer/>.
- **TCGA-BRCA:** The TCGA-BRCA dataset is used for training the BRCA-ODX stratification model. consisting of 1065 diagnostic WSIs with corresponding labels. It includes 312 high-risk slides and 753 low-risk slides. It is publicly accessible through the GDC portal (<https://portal.gdc.cancer.gov>).

- **OSUWMC-BRCA:** OSUWMC-BRCA dataset is an internal dataset that we used for testing the BRCA-ODX stratification model. It includes 147 high-risk slides and 847 low-risk slides. This dataset is not publicly available.
- **PANDA:** The PANDA dataset is used for training and testing the ISUP-grading model. It is one of the largest public resources for prostate cancer grading, includes 10,616 digitized prostate biopsy WSIs collected from multiple international centers. It is publicly available at <https://www.kaggle.com/c/prostate-cancer-grade-assessment>.
- **SPIDER-CRC:** The SPIDER-CRC is used for training and testing the CRC patch-level phenotyping model. It includes 63,989 training images and 13,193 testing images spanning 13 categories. It is publicly available at <https://huggingface.co/datasets/histai/SPIDER-colorectal>.
- **SPIDER-Breast:** The SPIDER-Breast is used for training and testing the breast cancer patch-level phenotyping model. It includes 80,858 training images and 12,034 testing images spanning 18 categories. It is publicly available at <https://huggingface.co/datasets/histai/SPIDER-breast>.

## Data Availability

All TCGA and CPTAC data are publicly available at <https://portal.gdc.cancer.gov>. DHMC-RCC dataset is available at <https://bmirds.github.io/KidneyCancer/>. PANDA dataset is available at <https://www.kaggle.com/c/prostate-cancer-grade-assessment>. SPIDER datasets are available at <https://huggingface.co/histai/datasets>.

## Code Availability

Our code and model weights are made available on <https://github.com/AI4Path-Lab/XMAG>.

## Acknowledgments

The project described was supported in part by R01 CA276301 (PIs: Niazi and Chen) from the National Cancer Institute, R01 DC020715 (PIs: Moberly and Gurcan) from the National Institute on Deafness and Other Communication Disorders, and R01 HL177046-01 (PIs: Hachem, Gurcan, and Michelson) from the National Heart, Lung, and Blood Institute. The project was also supported partly by Pelotonia under IRP CC13702 (PIs: Niazi, Vilgelm, and Roy), The Ohio State University Department of Pathology and Comprehensive Cancer Center. The content is solely the responsibility of the authors and does not necessarily represent the official views of the National Cancer Institute or National Institutes of Health or The Ohio State University.

## Supplementary materials

Table S1. NSCLC subtyping performance of different foundation models on CPTAC-NSCLC dataset. Averaged performance values and standard deviations across five-fold cross-validation are reported.

	Mag	Model size	Accuracy	F1	AUC
Phikon	20x	86M	0.855 $\pm$ 0.018	0.849 $\pm$ 0.011	0.945 $\pm$ 0.011
UNI2	20x	682M	0.860 $\pm$ 0.013	0.854 $\pm$ 0.013	0.951 $\pm$ 0.008
XMAG	5x	86M	0.845 $\pm$ 0.033	0.843 $\pm$ 0.023	0.941 $\pm$ 0.015

Table S2. RCC subtyping performance of different foundation models on DHMC dataset. ABMIL models are trained on the TCGA-RCC dataset and tested on the DHMC dataset. Averaged performance values and standard deviations across five-fold cross-validation are reported.

	Mag	Model size	Accuracy	F1	AUC
Phikon	20x	86M	0.903 $\pm$ 0.013	0.812 $\pm$ 0.017	0.969 $\pm$ 0.006
UNI2	20x	682M	0.958 $\pm$ 0.015	0.913 $\pm$ 0.021	0.989 $\pm$ 0.003
XMAG	5x	86M	0.953 $\pm$ 0.008	0.916 $\pm$ 0.015	0.986 $\pm$ 0.009

Table S3. Prostate cancer ISUP grading performance of different foundation models on PANDA dataset. Averaged performance values and standard deviations across five-fold cross-validation are reported.

	Mag	Model size	Accuracy	F1	AUC
Phikon	20x	86M	0.731 $\pm$ 0.009	0.674 $\pm$ 0.017	0.923 $\pm$ 0.002
UNI2	20x	682M	0.719 $\pm$ 0.010	0.666 $\pm$ 0.010	0.925 $\pm$ 0.004
XMAG	5x	86M	0.688 $\pm$ 0.010	0.632 $\pm$ 0.012	0.910 $\pm$ 0.003

Table S4. BRCA-ODX stratification performance of different foundation models on OSUWMC dataset. ABMIL models are trained on the TCGA-BRCA dataset and tested on the OSUWMC dataset. Averaged performance values and standard deviations across five-fold cross-validation are reported.

	Mag	Model size	Accuracy	F1	AUC
Phikon	20x	86M	0.785 $\pm$ 0.068	0.805 $\pm$ 0.048	0.781 $\pm$ 0.003
UNI2	20x	682M	0.826 $\pm$ 0.030	0.835 $\pm$ 0.022	0.780 $\pm$ 0.015
XMAG	5x	86M	0.845 $\pm$ 0.016	0.844 $\pm$ 0.007	0.776 $\pm$ 0.006

Table S5. Breast cancer ROI phenotyping performance of different foundation models on SPIDER-Breast dataset. We performed linear probing based on different models and report the performance based on the official testing set of SPIDER-Breast.

	Mag	Model size	Accuracy	F1	AUC
Phikon	20x	86M	0.861	0.863	0.992
UNI2	20x	682M	0.878	0.863	0.994
XMAG	5x	86M	0.878	0.816	0.988

Table S6. CRC ROI phenotyping performance of different foundation models on SPIDER-CRC dataset. We performed linear probing based on different models and report the performance based on the official testing set of SPIDER-CRC.

	Mag	Model size	Accuracy	F1	AUC
Phikon	20x	86M	0.892	0.891	0.994
UNI2	20x	682M	0.895	0.894	0.994
XMAG	5x	86M	0.828	0.827	0.990

## Reference

- 1 Tavolara, T. E., Su, Z., Gurcan, M. N. & Niazi, M. K. K. in *Seminars in Cancer Biology*. (Elsevier).
- 2 Song, A. H. et al. Artificial intelligence for digital and computational pathology. *Nature Reviews Bioengineering* **1**, 930-949 (2023).
- 3 Chen, R. J. et al. Towards a general-purpose foundation model for computational pathology. *Nature Medicine* **30**, 850-862 (2024).

4 Ma, J. *et al.* Towards a generalizable pathology foundation model via unified knowledge distillation. *arXiv preprint arXiv:2407.18449* (2024).

5 Xu, H. *et al.* A whole-slide foundation model for digital pathology from real-world data. *Nature* **630**, 181-188 (2024).

6 Lu, M. Y. *et al.* Data-efficient and weakly supervised computational pathology on whole-slide images. *Nature Biomedical Engineering* **5**, 555-570 (2021). <https://doi.org/10.1038/s41551-020-00682-w>

7 Zhang, H. *et al.* in *Proceedings of the IEEE/CVF Conference on Computer Vision and Pattern Recognition*. 18802-18812.

8 Hollon, T. C. *et al.* Near real-time intraoperative brain tumor diagnosis using stimulated Raman histology and deep neural networks. *Nature medicine* **26**, 52-58 (2020).

9 Zimmermann, E. *et al.* Virchow2: Scaling self-supervised mixed magnification models in pathology. *arXiv preprint arXiv:2408.00738* (2024).

10 Neary-Zajiczek, L. *et al.* Minimum resolution requirements of digital pathology images for accurate classification. *Medical Image Analysis* **89**, 102891 (2023).

11 Jin, L. *et al.* DeepDOF-SE: affordable deep-learning microscopy platform for slide-free histology. *Nature communications* **15**, 2935 (2024).

12 Hinton, G., Vinyals, O. & Dean, J. Distilling the knowledge in a neural network. *arXiv preprint arXiv:1503.02531* (2015).

13 Gou, J., Yu, B., Maybank, S. J. & Tao, D. Knowledge distillation: A survey. *International journal of computer vision* **129**, 1789-1819 (2021).

14 Dooper, S. *et al.* Gigapixel end-to-end training using streaming and attention. *Medical Image Analysis* **88**, 102881 (2023).

15 Yu, J. *et al.* Exploring multi-instance learning in whole slide imaging: Current and future perspectives. *Pathology-Research and Practice*, 156006 (2025).

16 Ilse, M., Tomczak, J. & Welling, M. in *International conference on machine learning*. 2127-2136 (PMLR).

17 Filioit, A. *et al.* Scaling self-supervised learning for histopathology with masked image modeling. *MedRxiv*, 2023.2007. 2021.23292757 (2023).

18 Zhu, M. *et al.* Development and evaluation of a deep neural network for histologic classification of renal cell carcinoma on biopsy and surgical resection slides. *Scientific reports* **11**, 7080 (2021).

19 Bulten, W. *et al.* Artificial intelligence for diagnosis and Gleason grading of prostate cancer: the PANDA challenge. *Nature medicine* **28**, 154-163 (2022).

20 Su, Z. *et al.* Computational Pathology for Accurate Prediction of Breast Cancer Recurrence: Development and Validation of a Deep Learning-based Tool. *Modern Pathology*, 100847 (2025).

21 Guo, Y. *et al.* BPMambaMIL: A Bio-inspired Prototype-guided Multiple Instance Learning for Oncotype DX Risk Assessment in Histopathology. *Computer Methods and Programs in Biomedicine*, 109039 (2025).

22 Nechaev, D., Pchelnikov, A. & Ivanova, E. SPIDER: A Comprehensive Multi-Organ Supervised Pathology Dataset and Baseline Models. *arXiv preprint arXiv:2503.02876* (2025).

23 Maaten, L. v. d. & Hinton, G. Visualizing data using t-SNE. *Journal of machine learning research* **9**, 2579-2605 (2008).

24 Esmaeilzadeh, P. Challenges and strategies for wide-scale artificial intelligence (AI) deployment in healthcare practices: A perspective for healthcare organizations. *Artificial Intelligence in Medicine* **151**, 102861 (2024).

25 Le Fevre, E. M. & Heleg, G. in *Artificial Intelligence in Cardiothoracic Imaging* 527-534 (Springer, 2022).

26 Dosovitskiy, A. *et al.* in *International Conference on Learning Representations*.

27 Deng, R. *et al.* in *Proceedings of the IEEE/CVF conference on computer vision and pattern recognition*. 11736-11746.

28 Kömen, J. *et al.* Towards Robust Foundation Models for Digital Pathology. *arXiv preprint arXiv:2507.17845* (2025).

29 Oquab, M. *et al.* DINOv2: Learning Robust Visual Features without Supervision. *Transactions on Machine Learning Research Journal*, 1-31 (2024).